International Journal of Multiphase Flow 136 (2021) 103541

Contents lists available at ScienceDirect

International Journal of Multiphase Flow

journal homepage: www.elsevier.com/locate/ijmulflow

Bubble drag in electrolytically generated microbubble swarms with bubble-vortex interactions

Yasunori Watanabe[a,*], Haruhi Oyaizu[b], Hisashi Satoh[a], Yasuo Niida[c]

[a] Hokkaido University, School of Engineering, North 13 West 8, Sapporo, Japan
[b] MODEC, Inc., Engineering Department, Nihonbashi Maruzen Tokyu Building, 3-10, Nihonbashi 2-chome, Chuo-Ku, Tokyo, Japan
[c] Environmental Science Research Laboratory, Central Research Institute of Electric Power Industry, Abiko, Chiba, Japan

ARTICLE INFO

Article history:
Received 17 February 2020
Revised 11 August 2020
Accepted 7 December 2020
Available online 13 December 2020

Keywords:
Microbubbles
Bubble drag
Bubble–vortex interaction

ABSTRACT

Air bubbles entrained in ocean breaking waves play various roles in air–sea gas transfer, wave energy dissipation, and surface layer mixing. While sub-mm bubbles dominate the distribution of sizes observed in bubble plumes created by breaking waves, the dynamics of such microbubbles in a swarm are poorly understood, and most previous experimental and computational studies have focused on the behavior of homogeneous swarms of larger mm-scale bubbles for industrial applications. Here, we propose novel probabilistic empirical models of rise velocity and bubble drag for a microbubble swarm incorporating bubble–vortex interactions. These are based on image measurements of the motion of electrolytically generated microbubbles. We found that convective interactions between bubbles and vortex-induced flows, that is, Rayleigh–Taylor instability caused by density difference near the electrodes, induce counter-rotating vortices that accelerate bubbles and align them along paths in the flow induced between them, resulting in an increase in rise velocity and its variance in the statistical equilibrium state. We describe the statistical features of bubble rise in such swarms in our proposed empirical model and deduce its optimal parameters. We anticipate our findings being a starting point for understanding behaviors of oceanic bubbles possessing an analogous size distribution to the present electrolytically generated microbubbles.

1. Introduction

Breaking waves in the ocean entrain air bubbles into a surface layer, which aerates seawater, providing a variety of contributions to the ocean environment through air-sea gas exchange (Jähne and Haußecker, 1998; Melville, 1996). Wallace and Wirick (1992) observed correlations between ocean wave height and saturation of dissolved oxygen in the ocean surface, indicating a direct contribution of breaking-wave-induced bubbles to gas transfer. Farmer et al. (1993) found that conventional gas transfer coefficients underestimate the observed gas transfer during periods of bubble penetration; bubble entrainment is an important factor for predicting the air–sea gas flux.

The mechanical effects of entrained bubbles on ocean waves, resulting in energy dissipation, have also been studied (Melville, 1996). Lamarre and Melville (1991) observed that half of breaking wave energy was dissipated via bubble entrainment. Melville and Matusov (2002) used aerial images of whitecaps to estimate data related to the lengths of breaking crests, defining momentum flux and energy dissipation. Callaghan et al. (2012) found correlations between whitecap foam decay time and maximum foam patch area, which parameterizes wave energy dissipation (Callaghan et al., 2012). Whitecap timescale has also been related to sea spray aerosol production through a bursting process, which occurs when the buoyant bubbles reach the ocean surface (Callaghan, 2013).

These aeration effects strongly depend on bubble size distribution as well as bubble population in seawater. Vagle and Farmer (1992) used a multi-frequency acoustical backscatter technique to estimate bubble size distributions at different depths off the coast of California. They found a logarithmic spectrum slope for bubble sizes larger than the peak radius ($a \approx 20$–30 μm); it varied from less than a^{-4} close to the ocean surface to a^{-7} at the bottom of the bubble cloud. Farmer et al. (1998) collected observations in the Gulf of Mexico using a free-flooding acoustic resonator. They found that the dominant bubble size, achieving the maximum

* Corresponding author.
E-mail address: yasunori@eng.hokudai.ac.jp (Y. Watanabe).

https://doi.org/10.1016/j.ijmultiphaseflow.2020.103541

air fraction below the ocean surface, had a diameter range of 80–200 μm. Deane and Stokes (2002) found that the power-law scaling of the bubble size spectrum changes at a critical scale, called the Hinze scale $a_H \approx 1$ mm, defined by the bubble breakup length caused by turbulence; that is, a time-averaged spectrum slope of $a^{-3/2}$ for $a < a_H$ and $a^{-10/3}$ for $a > a_H$. They also observed that the Hinze scale applies in the open ocean for the variable spectrum slopes according to plume age. The initial slopes $a^{-1.8}$ $(a < a_H)$ and $a^{-4.9}$ $(a > a_H)$ become steeper with increasing time and decreasing void fraction because large bubbles, with buoyancy that dominates over drag, rapidly ascend and disappear through buoyant degassing, while smaller bubbles are involved in turbulence and are passively transported at depth (Deane and Stokes, 2002; Melville, 1996). In the surf zone, an organized vortex structure, composed of primary horizontal rollers enveloped by rib vortices, is produced during the wave breaking process (Watanabe et al., 2005; Otsuka et al., 2017), which forms bubble plumes along the rib vortices, in which bubbles are entrapped and remain for a long time, against buoyant degassing. As residence time of air within these vortices increases, gas dissolution into seawater enhances (Niida and Watanabe, 2018).

The dynamics of a single bubble ejected from a submerged needle in still water has been extensively investigated in laboratory experiments (Oguz and Prosperetti, 1993; Tomiyama et al., 2002; Niida and Watanabe, 2018). Because bubble detachment from the needle requires that the bubble's buoyancy prevails against its surface tension with the needle wall, this method can produce only a large bubble, typically larger than 2 mm in diameter. Large bubbles, generally possessing deformed shapes with high aspect ratios (Clift et al., 1978) due to vortices generated behind the lower surface, ascend with lateral fluctuations along zigzag or helical paths (Tomiyama et al., 2002; Niida and Watanabe, 2018), which agitates fluid flow and modifies the statistics of the turbulence (Risso, 2018). Experimental drag models for a needle-generated isolated bubble in quiescent water have been developed for various ranges of parameters, including Eotvos $E_o(=\rho g d^2/\gamma)$, Moton, $M=(g\mu^4/\rho\gamma^3)$, and Reynolds numbers $Re(=\rho d u_t/\mu)$, where ρ, g, d, γ, u_t, and μ are the liquid density, gravitational field strength, bubble diameter, surface tension, terminal velocity, and viscosity, respectively (Clift et al., 1978). Tomiyama et al. (1998) integrated the previous models of bubble drag over the different parameter ranges, and proposed a universal empirical drag coefficient, which includes the effects of bubble deformation and surfactants and covers the ranges: $10^{-2} < E_o < 10^3$, $10^{-14} < M < 10^7$ and $10^{-3} < Re < 10^5$.

Consecutive bubble ejection from an array of needles or capillary tubes form a homogeneous bubble swarm, and this phenomenon has been statistically analyzed in terms of void fraction (Risso, 2018). Simonnet et al. (2007) measured relative bubble velocity in a swarm in a range for d of 2–10 mm and for a void fraction of $\alpha < 35\%$. They found that bubble drag increases with α, due to a hindrance effect at $\alpha < 15\%$ whereby aspiration of bubbles in the wake of proceeding ones may reduce bubble drag for higher α. Colombet et al. (2015) observed a slower bubble rise in a swarm than for a single bubble, due to the hindrance effect. Roghair et al. (2011) computationally studied the α-dependent drag of randomly arrayed bubbles in the range for d of 1–7 mm and discussed the effects of bubble clusters on bubble drag, noting that it increases with α and decreases with E_o (Roghair et al., 2013). Smereka (1993) found that bubble clusters are formed in uniform bubble flows with less velocity fluctuation, and that bubble-induced agitation may prevent cluster formation. While previous research has clarified the major mechanical features of homogeneous swarms of large bubbles (Risso, 2018), the dynamics of sub-mm scale bubbles, as observed in aerated ocean surfaces, are poorly understood because smaller bubbles cannot be created by conventional methods, which involve the use of needles or capillary tubes.

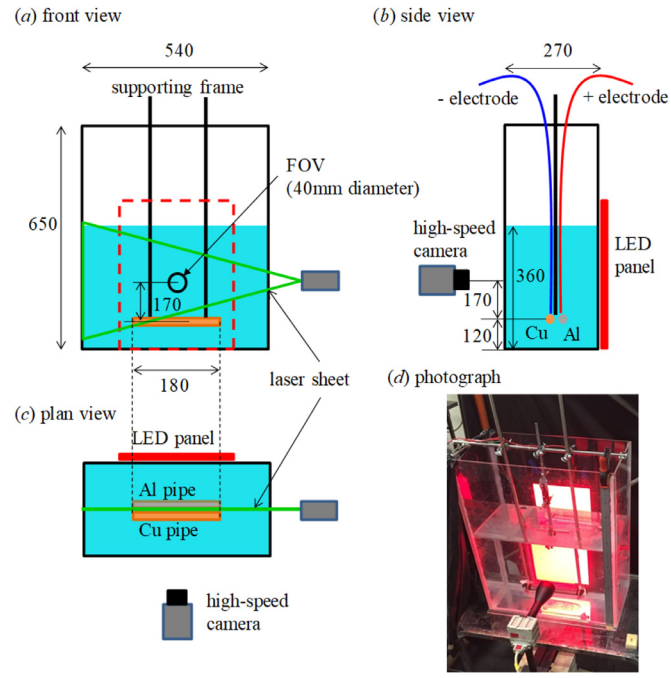

Fig. 1. Experimental setup for measurement images of electrolytic bubbles. (*a*) Front view of the tank, (*b*) side view, (*c*) plan view (unit: mm) and (*d*) photograph of the backlit measurement system.

Electrolysis of water can generate smaller bubbles in a diameter range of 10–1000 μm, which covers the dominant oceanic bubble size. The dynamics of electrolytic bubbles may help clarify the mechanical effects of entrained microbubbles in ocean waves. In this study, we performed a high-resolution image analysis to explore any distinctive geometrical and dynamic features of electrolytically generated microbubble swarms, with the goal of clarifying the collective effects of bubble drag in microbubble swarms, as a first step toward the mechanical modeling of similar ocean bubbles.

The remainder of this paper is organized as follows. Section 2 presents the experimental setup for generating electrolytic bubble swarms and methods for their analysis. Section 3 characterizes the observed bubble size distributions of the electrolytic microbubbles. Section 4 discusses the collective effects causing the transition of bubble motions. Section 5 proposes novel bubble rise and drag models for microbubble swarms in a statistically equilibrium state. Finally, Section 6 summarizes all of the findings.

2. Laboratory experiment

Laboratory experiments were performed in a rectangular transparent tank 540 mm long, 270 mm wide, and 650 mm high (Fig. 1). A copper pipe and an aluminum pipe, both with a diameter of 10 mm and a length of 180 mm, were placed in parallel, with 3 mm spacing, 100 mm above the bottom of the tank and submerged in 0.2% sodium chloride solution, filled to a depth of 360 mm. The copper pipe and aluminum pipe were connected to a DC power supply, as cathode and anode, respectively, and hydrogen microbubbles were created by electrolysis of the water at electric currents, I = 7.5, 10.0, 15.0, and 20.0 A. The bubbles were illuminated by a red light emitting diode (LED) light panel (410 mm ×230 mm) through the (transparent) rear tank wall. Backlit shadow images of bubbles were recorded by a high-speed digital video camera (resolution, 1280 × 1024 pixels), equipped

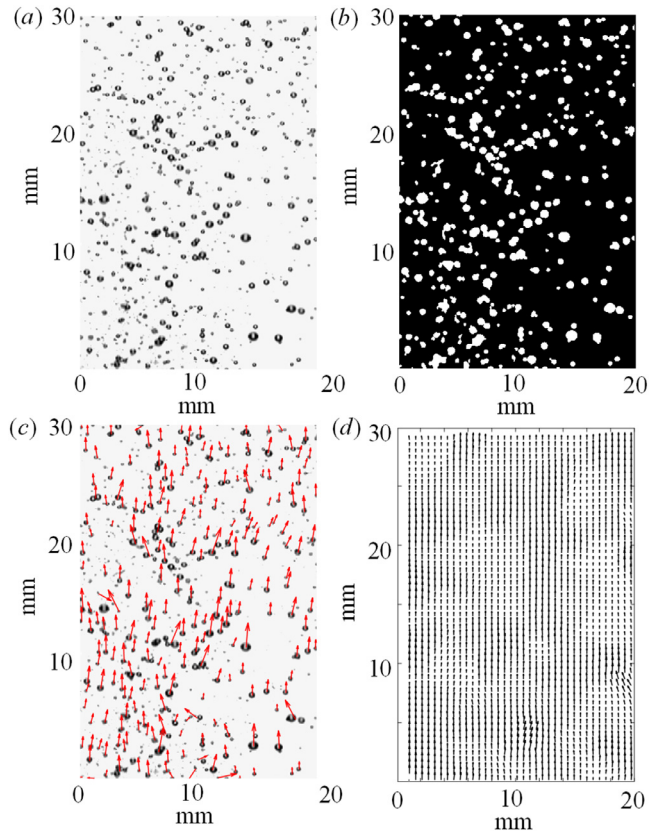

Fig. 2. Examples of (*a*) a bubble image used for analysis, (*b*) a binary bubble image, based on level-set edge detection, (*c*) measured bubble velocities, and (*d*) a measured liquid-velocity distribution.

with a telecentric lens, in front of the tank, 170 mm above the electrodes, with a recording frequency of 250 Hz. The original eight-bit images of bubbles within a 40-mm circular field of view (FOV) in the telecentric optical system were acquired at a resolution of 25.6 pixel/mm. Unresolved bubbles, smaller than 80μm, were not included in our analysis. Images in a region of 20 mm × 30 mm in the center of the FOV were used for the analysis (see Fig. 2*a*).

The shape of these experimental microbubbles (typically with $R_e \sim 10^2$ and $E_o \sim 10^{-2}$ was well approximated as spherical (Clift et al., 1978). Thus, bubble size was evaluated as an equivalent circle diameter, d, for each area whose interface was detected by a level-set method (Fig. 2*b*) in the same manner as that used by Niida and Watanabe (2018). Bubbles located out of the focal plane were identified using the gradient of the image intensity at each bubble's interface and removed from the analysis. Overlapped bubble images were defined as those with an aspect ratio (height-to-width ratio) of shadow shape surrounded by an interface smaller than 0.8. To avoid erroneous bubble size estimation caused by overlaps of bubbles along the backlit rays, these were also removed from the statistics. We defined the time, t, from the instant when the first bubble was detected in the measurement region.

In this paper, I is used as a measure of the void fraction in the electrolysis bubble flows as volume of the hydrogen gas generated per unit time and area increases with I. The void fraction α was estimated by using the measured size distributions as $\alpha = \pi \sum d_i^3/6DH$, where d_i is the equivalent circle diameter of the recorded ith bubble, D is the image area for measurement (600 mm^2), and H is the depth of field (10 mm).

Niida and Watanabe (2018) measured the bubble rise velocity in bubble plumes by tracking bubble centers, and measured the liquid velocity in the plumes via super-resolution particle imaging velocimetry (SRPIV, see Keane et al. (1995)). In general, while bubble tracking is straightforward and useful for estimating the velocity of individual bubbles, mismatching with adjacent bubbles may cause tracking errors, especially in populated areas. SRPIV, a hybrid technique of cross-correlation particle imaging velocimetry and particle tracking velocimetry for tracers in flows, significantly reduces mismatching errors in the tracking procedure by selecting candidate particle trajectories across each frame via a cross-correlation method, which provides optimal tracking velocities even in dense particle fields. In the current experiment, microbubble velocity was estimated using the same framework as SRPIV but using images of bubbles instead of seeded particles. In this framework, the candidate bubble velocity in a rectangular window containing 64 × 64 pixels was estimated using a cross-correlation method, which corresponds with that used in the bubble imaging velocimetry technique proposed by Ryu et al. (2005). Assuming local steady flow over sequential frames, bubble centers were then tracked in the direction of the candidate bubble velocity over three sequential images to select the optimal bubble trajectory with the lowest error. The bubble velocity, $\boldsymbol{v}_b(i,t)$, for the ith bubble was estimated along the determined trajectories over sequential frames (Fig. 2*c*).

Another experiment, to measure liquid velocity, $\boldsymbol{u}(\boldsymbol{x},t)$, was performed under identical bubble conditions (see Niida and Watanabe (2018) for details of the method). In this experiment, neutrally buoyant fluorescent particles of approximately 20 µm in diameter were used as tracers for the liquid flow. A continuous wave YAG laser sheet was installed level with the measurement section, above the electrode pipes, outside the transparent side wall of the tank (see Fig. 1). Laser light (with a wavelength of 532 nm) was reflected from the bubble surfaces. A camera was equipped with a high-pass optical filter (cut-off wavelength, 580 nm), which prevented it from recording the reflected light, capturing only the laser-induced fluorescent light (peak wavelength, 650 nm) emitted by the fluorescent tracers. Eight-bit particle images recorded by the high-speed camera were stored as uncompressed bitmaps on a PC connected to the camera. Image noise was reduced by median filtering. The planar distribution of particle velocities was computed using SRPIV (Fig. 2*d*).

The relative rise velocity of the ith bubble with respect to $\boldsymbol{u}$ is defined by $\boldsymbol{v}_r(i,t) = \boldsymbol{v}_b(i,t) - \overline{\boldsymbol{u}(\boldsymbol{x},t)}$, where $\overline{\boldsymbol{u}(\boldsymbol{x},t)}$ is $\boldsymbol{u}$ averaged over the measurement area (20 mm × 30 mm), as used for the analysis in Section 5.

In addition to the SRPIV measurements of microscale bubble and liquid motions within the small domain 20 mm × 30 mm, macroscale structures of bubble swarms were also visually observed over a deeper depth 520 mm in another rectangular tank (200 mm long × 200 mm width × 700 mm height), which is explained in the next section.

3. Evolution of electrolysis bubble swarms

In this section, overall features of macro-structures of electrolysis bubble swarms are introduced, before quantitatively discussing local bubble and liquid motions, acquired by high-resolution measurements in the following sections.

Fig. 3 shows the macro side view of a microbubble swarm over the depth and the macro shadow image of the swarms along the electrode. We found a distinctive transition of bubble motion in the swarm (see also supplemental movie 1): bubbles produced on the electrode ascend along straight rising paths in the early stage, forming a planar swarm with uniform thickness (Fig. 3*a*), while bubble wakes occur, varying the lateral thickness of the swarm

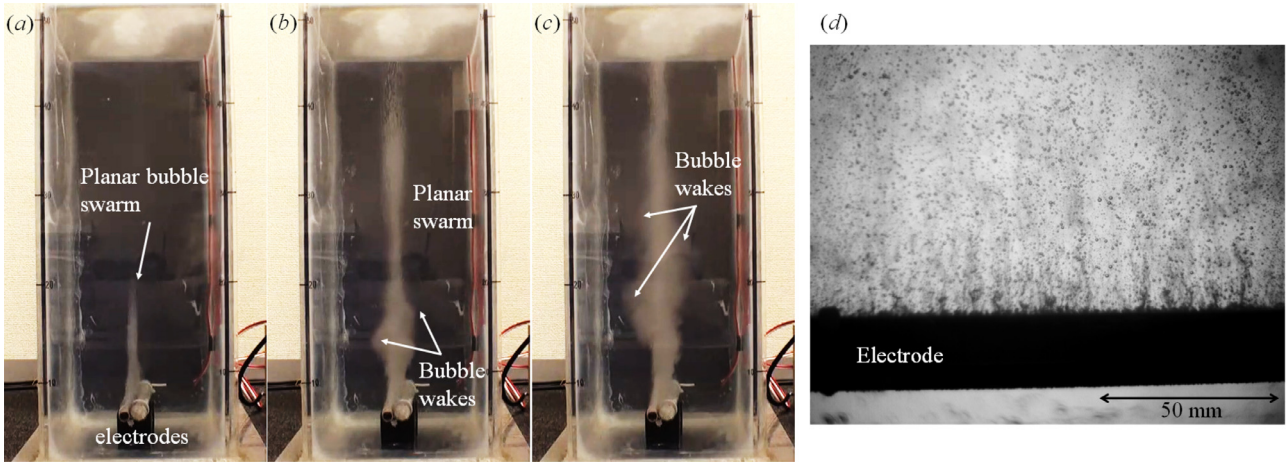

Fig. 3. Macro side view of an electrolytically created microbubble swarm at (*a*) 0.868 s, (*b*) 3.10 s and (*c*) 5.44 s after starting electrolysis, and (*d*) a macro shadow image of the microbubbles generated along the electrode, wherein a striped pattern is visible (indicating the locations with high population), caused by Rayleigh–Taylor instability.

as bubble concentration increases (Fig. 3*b*, *c*). We observed striped patterns of bubble shadows, indicating regular transverse variations in their concentration along the electrode (Fig. 3*d* and supplementary movie 2), which might be induced by the Rayleigh–Taylor instability, induced by the difference in mean ρ between the liquid and bubble layers on the electrode. As bubble ejection with regular wavelength of 5–10 mm on the electrode developed (mean wavelength about 7 mm), buoyancy-induced upweling flows might successively create vortices to release upward. The vortex-induced flows might affect bubble motion to align bubbles on oscillatory bobble paths for forming cell-wall-like clusters (supplementary movie 2). A similar vortex-induced bubble clusters formed in a thin liquid layer has been computationally observed by Climent and Magnaudet (1999).

The local bubble behaviors in the transitional large-scale organization of flows, induced in the Rayleigh-Taylor process, are quantitatively discussed again in Section 5.

4. Bubble size distribution

Electrolysis of water creates non-uniform sizes of microbubbles, unlike the previous experiments for homogeneous bubble swarms produced by needle arrays. Here, we define the fundamental geometrical properties of the electrolytic microbubbles used in our experiment. As mentioned in Section 3, electrolytic bubble swarms change in form with increasing population. Bubble size distributions in the statistical equilibrium state, when a quasi-steady α is achieved, are discussed in this section (details of the transitions of bubble swarms will be discussed in the following sections).

Fig. 4 presents histograms of d of electrolytically generated bubbles for I = 7.5, 10, 15, and 20 A. The highest number density is observed for $d = 300 - 500$ µm. Each histogram has a tail toward large d. The tails become larger with increasing I, and the mean bubble diameter, d_m, also monotonically increases with I: d_m = 0.521 mm for I = 7.5A, 0.541 mm for 10.0 A, 0.594 mm for 15.0 A, and 0.631 mm for 20.0 A. It should note that the void fraction also increases with I, α = 0.42% (I = 7.5 A), 0.43% (I = 10 A), 0.54% (I = 15 A) and 0.59% (I = 20 A), which causes increase of the ensemble mean bubble velocity as $\langle v_b \rangle$ = 126.4 mm/s for I = 7.5 A, 138.1 mm/s for 10 A, 151.4 mm/s for 15 A, and 180.7 mm/s for 20 A.

Probability densities describing asymmetrical distributions with tails include: the Γ distribution,

$$p_\Gamma(x = d/d_m) = \frac{n^n}{\Gamma(n)} x^{n-1} \exp(-nx); \tag{1}$$

the Weibull distribution,

$$p_W(x) = \frac{\beta}{\alpha}\left(\frac{x}{\alpha}\right)^{\beta-1} \exp\left(-\left(\frac{x}{\alpha}\right)^{\beta}\right), \tag{2}$$

where the parameters α (which should not be confused with void fraction) and β are estimated empirically, and the lognormal distribution,

$$p_{ln}(x) = \frac{1}{x\sigma\sqrt{2\pi}} \exp\left(\frac{-(\ln x - \mu)^2}{2\sigma^2}\right), \tag{3}$$

where the logarithmic average, μ (which should not be confused with viscosity), and standard deviation, σ, are determined by fitting procedures.

Fig. 5 presents a comparison of the probability density distributions of the measured bubble size for the Γ, Weibull, and lognormal distributions with optimal parameters. All of the Γ distributions fail to model the smaller sizes, d/d_m <0.5, and underestimate the maximum probability density, although bubbles larger than the mean, $d/d_m > 1$, are approximated well by Γ (n = 5). The Weibull distribution did not approximate the probabilities well for any bubble sizes. We found that the lognormal distribution models the measured one well over the whole range, that is, the electrolytic microbubble size is best described statistically by the lognormal distribution.

The maximum likelihood estimates of μ and σ for the lognormal distribution (3) as a function of I are provided in Fig. 6.

Deane and Stokes (2002) found that during wave breaking events, bubble size follows a slope of −3/2 for the time-averaged spectrum for $a < a_H \approx 1$ mm, and a slope of −10/3 for $a > a_H$. They also observed two different slopes in the time-dependent size spectrum in open ocean: $a^{-1.8}$ for $a < a_H$ and $a^{-4.9}$ for $a > a_H$ when bubble plumes developed. We found that the two slopes characterize the experimental spectrum of bubble size for a larger than the dominant radius, $a > a_{\max} \approx 200$ µm: a slope of −1.5 for $a_{\max} < a < a_H$ (broken line in Fig. 7) and of −4.4 for $a > a_H$ (solid line), where the inflection radius, a_H, varies from about 300–400 µm with I. The $a^{-1.5}$ spectrum for smaller than a_H is consistent with those observed in the laboratory ($a^{-3/2}$) and open ocean ($a^{-1.8}$) by Deane and Stokes (2002), while the $a^{-4.4}$ spectrum is similar to the observations of Deane and Stokes ($a^{-4.9}$), Vagle and Farmer (1992) (a^{-4}), and Johnson and Cooke (1979) ($a^{-4.5}$), suggesting that the microbubbles produced and analyzed in this study have comparable geometrical features to ocean bubbles.

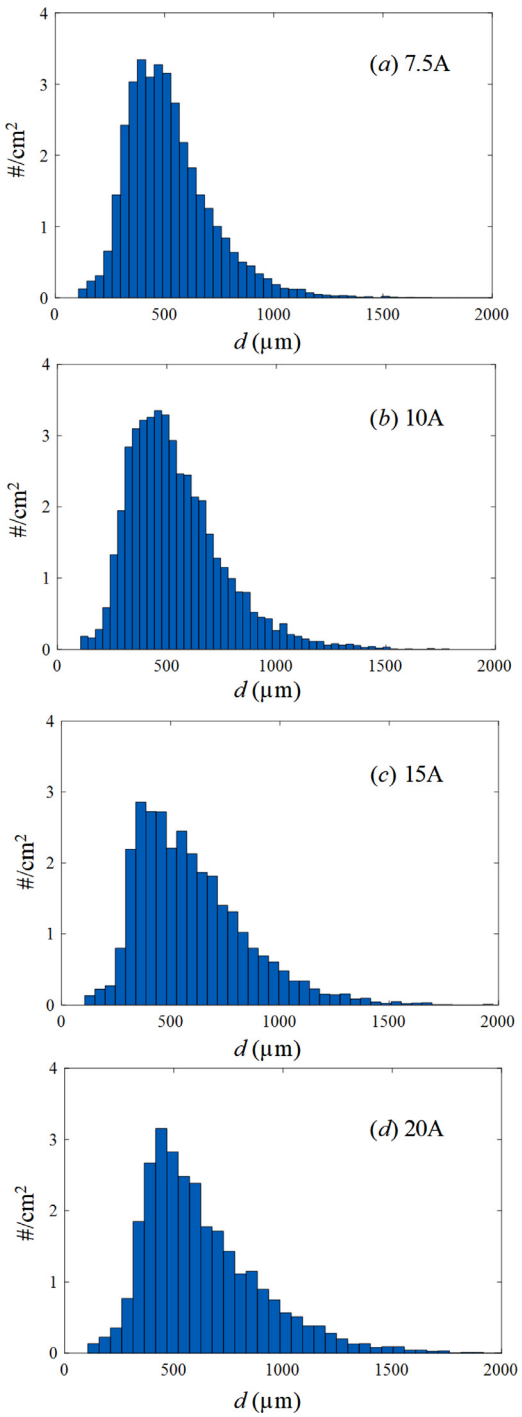

Fig. 4. Histograms of electrolytic bubble diameters for current, I = (a) 7.5, (b) 10, (c) 15, (d) 20 A.

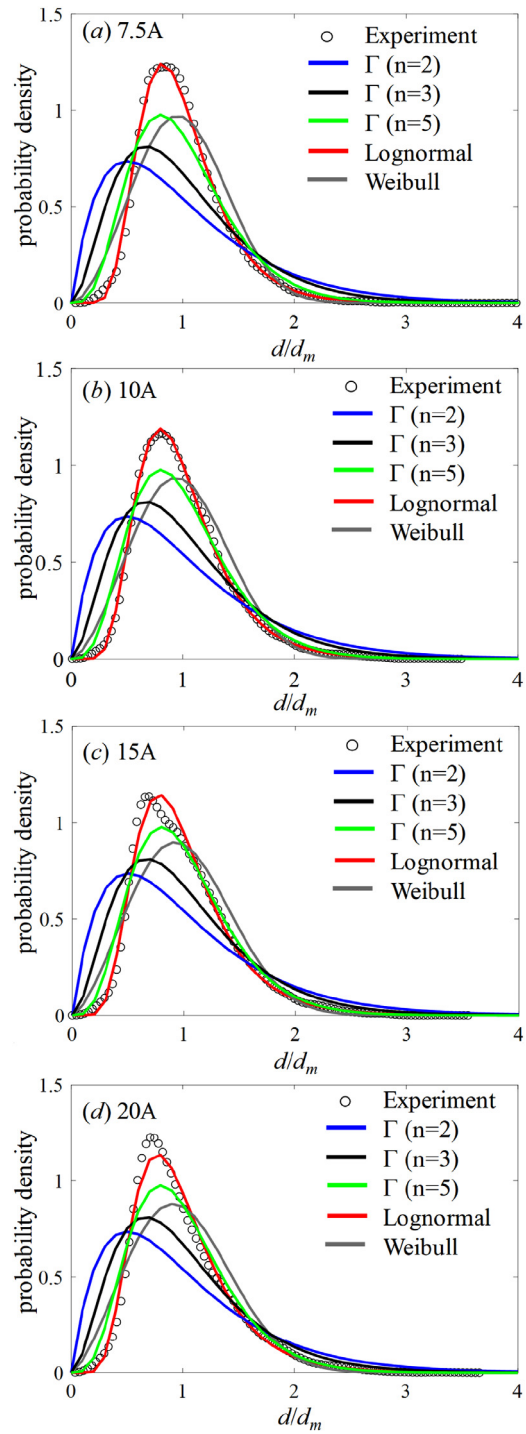

Fig. 5. Probability densities for bubble size normalized by the mean diameter, d_m, for currents of (a) 7.5, (b) 10, (c) 15, and (d) 20 A.

5. Microbubble motion in swarms

Fig. 8 presents the temporal variations of micro-structures of the bubble swarm. The randomly located bubbles ascend at their own terminal rise velocities along simple, straight trajectories in the early stage (a, supplementary movie 3), while lateral bubble motion begins appearing when the population increases shortly after (b, supplementary movie 4). With a further increase in population, the bubbles begin to locally align, forming cell-wall-like clusters after $t \approx 2.5$ s (c–f), while lateral undulations amplify (supplementary movie 5).

Fig. 9 presents the temporal evolution of the measured instantaneous $\mathbf{v}_b$, and the vertical and horizontal components of $\boldsymbol{u}$ for I = 15 A. It should be noted that the liquid flow was separately measured from the bubble flow experiment (see section 2), so the instantaneous velocity distribution of bubbles does not correspond to those of the liquid flows. We found local disturbances in the vertical component of $\boldsymbol{u}$, which may be caused by bubble agitations, increasing with bubble population in the early stage (a–b), and then concentrated 'patches' sequentially pass upward in later phases (c–e). While there are very minor agitations in the hori-

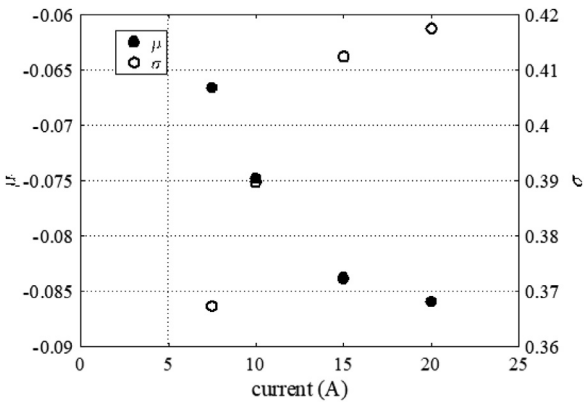

Fig. 6. Optimal parameters, μ and σ, of the lognormal distribution as a function of current.

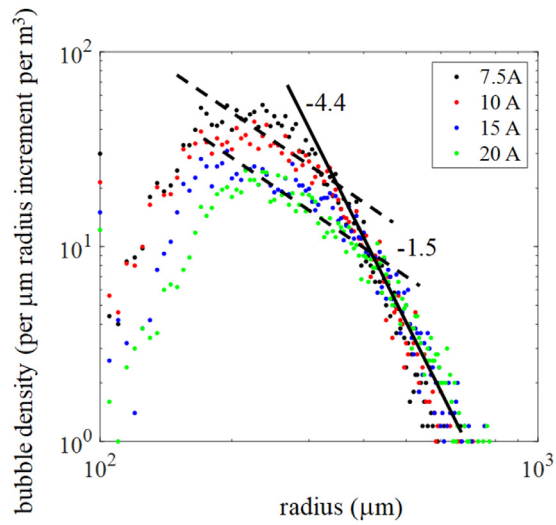

Fig. 7. Bubble size spectrum (number of bubbles per m^3 binned by radius, each 1 μm wide). Solid and broken lines indicate slopes of −4.4 and −1.5, respectively.

zontal component of **u**, locally induced in the early stage, positive and negative horizontal flows rapidly intensify over larger areas after that phase (*c*), caused by large-scale vortices formed by the Rayleigh–Taylor process. The vortex-induced horizontal divergent and convergent flows contribute to locally sweeping and aggregating bubbles in clusters observed in Fig. 8.

Fig. 10 shows the measured distributions of instantaneous liquid vorticty at sequential phases for $I = 15$ A. We found that multiple pairs of counter-rotating vortices, interacting with the adjacent pairs for being locally displaced and deformed, are transported upward by buoyancy-induced flow. The vortex pairs may organize a steric structure as the vorticity temporally varies with the out-of-plane displacement. The separation distance between each pair of the counter-rotating vortices, l_p (distance between broken circles in Fig. 10), is estimated in a range of 5–10 mm, which coincides with the observed unstable wavelength on the electrode (Fig. 3), ensuring the observed counter-rotating vortices developed in the Rayleigh-Taylor process.

Fig. 11 schematically illustrates typical bubble motion in the system involving counter-rotating vortices observed in the experiments. As explained in Section 3, a striped pattern of bubble shadows (indicating high bubble concentration) near the electrode (Fig. 3*d* and supplementary movie 2) was caused by Rayleigh–Taylor instability. The undulation of bubble accumulation amplifies and vertically ejects bubbles at regular intervals, corresponding to the most unstable wavenumber on the electrode, resulting

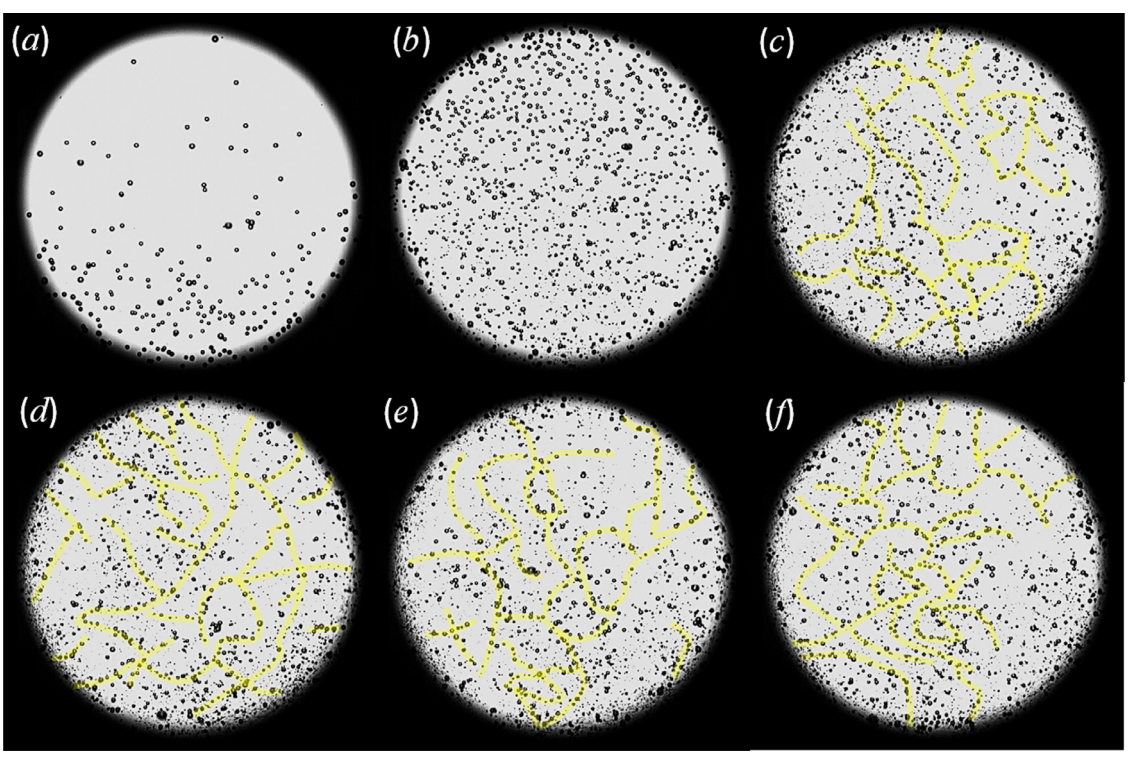

Fig. 8. Backlit images of bubbles at t = (*a*) 0.552, (*b*) 1.160, (*c*) 2.624, (*d*) 2.748, (*e*) 2.808, and (*f*) 2.920 s after starting electrolysis. The images were recorded with resolution of 25.6 pixels/mm at 170 mm above the electrodes (see Fig. 1). The diameter of a circular FOV is about 40 mm. Random bubble arrangements at the early stage (*a* and *b*) evolve into rectilinear arrangements forming cell-wall-like clusters (*c*–*f*). The yellow lines indicates traced bubble alignments. (For interpretation of the references to color in this figure legend, the reader is referred to the web version of this article.)

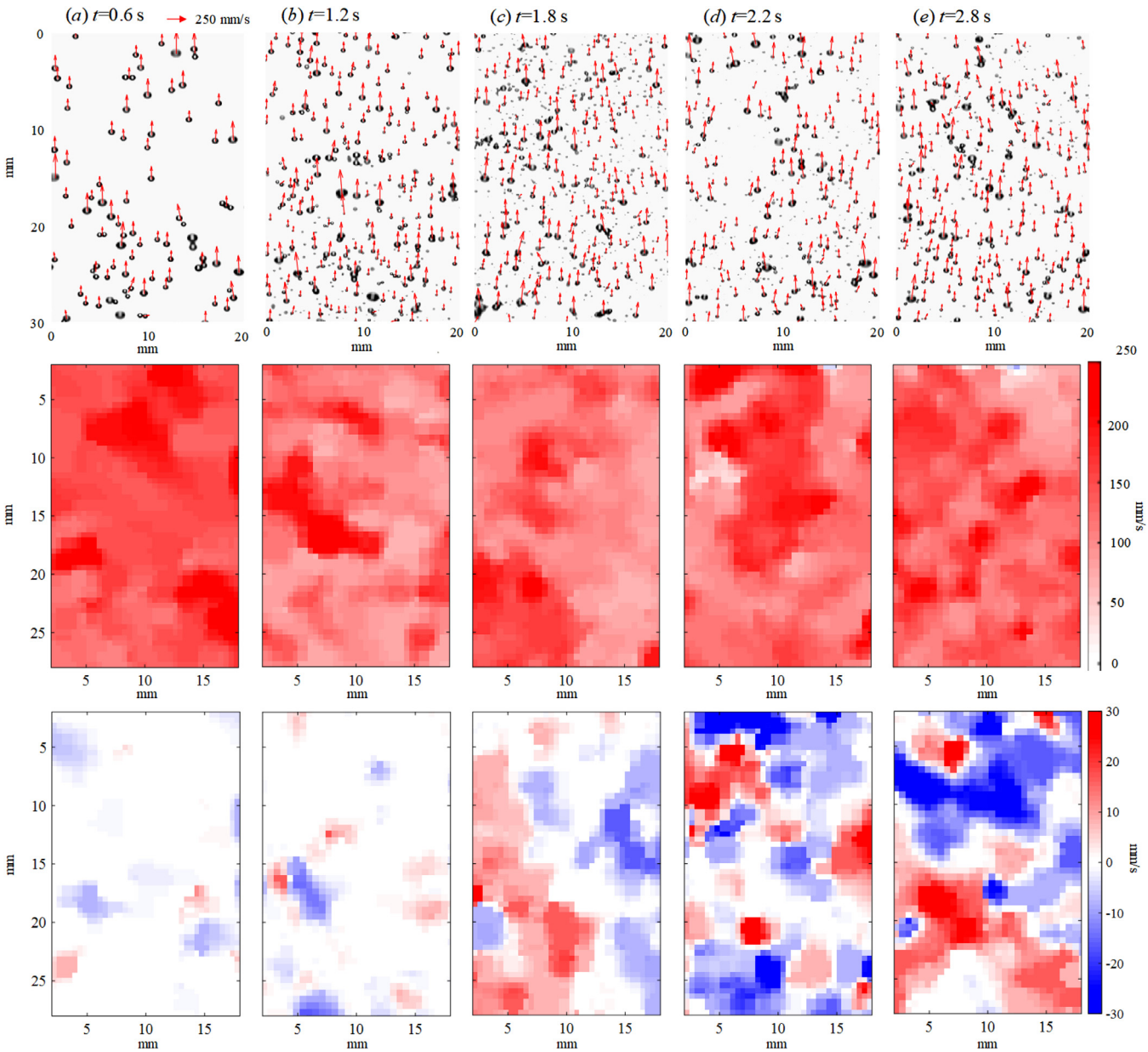

Fig. 9. Distributions of (top) bubble, (middle) vertical liquid, and (bottom) horizontal liquid velocities for a current of 15 A at t = (*a*) 0.6, (*b*) 1.2, (*c*) 1.8, (*d*) 2.4, and (*e*) 3.0 s.

in buoyancy-driven upwelling liquid flows, which induces formation of counter-rotating vortices above the ejections as observed in Fig. 10. In addition to the buoyancy-induced bubble rise, vortex-induced liquid flows may affect local bubble motions: bubbles accumulated by the convergent flows (where bubble paths merged in Fig. 11), are carried by the intensified, ascending flow between the vortices. The bubbles may align along oscillatory paths in the vortex-induced flows for forming the cell-wall-like clusters observed in Fig. 8.

Since the vortices, inducing flows with fluctuation velocity $\boldsymbol{u}'$ between them (Fig. 9), carried upward by the buoyancy-induced mean flow with $\overline{\boldsymbol{u}}$ (Fig. 10), the bubbles should be accelerated in the flow with $\boldsymbol{u}' + \overline{\boldsymbol{u}}$ between the vortices, which may attains faster bubble velocity than the single bubble rise without any vorticity effect.

These bubble-vortex interactions in a flow system involving multiple counter-rotating vortices, created by the Rayleigh-Taylor instability, are quantitatively examined in terms of time- and length-scales of bubble and liquid velocities. We computed the Eulerian autocorrelation for liquid velocity projected to the horizontal ($j = 1$) and vertical ($j = 2$) directions (Squires and Eaton, 1991);

$$R_{Ej} = \frac{\overline{u_j'(\mathbf{x})u_j'(\mathbf{x} + r\mathbf{e}_j)}}{\overline{u_j'^2}} \tag{4}$$

where the velocity fluctuation $u_j' = u_j - \overline{u_j}$ ($\overline{u_j}$ is the spatial mean velocity), and $\boldsymbol{e}_j$ is the unit vector in each direction, i.e. horizontal and vertical translations $(\xi, \zeta) = (r\boldsymbol{e}_1, r\boldsymbol{e}_2)$.

Fig. 12 shows R_{E2} and R_{E1} at sequential phases (see also the corresponding phases in Fig. 10). We found oscillatory behaviors in R_{E2} with respect to the vertical translation ζ (Fig. 12 top). As the negative minima of R_{E2} at $\zeta = l_2^- \sim 3$ mm indicates presence of the opposite flow there, we define the length l_2^-, achieving the minimum value, characterizing a distance between divergent and convergent flows (Fig. 9). The vertical separation distance between the vortex pairs, inducing the identical orienta-

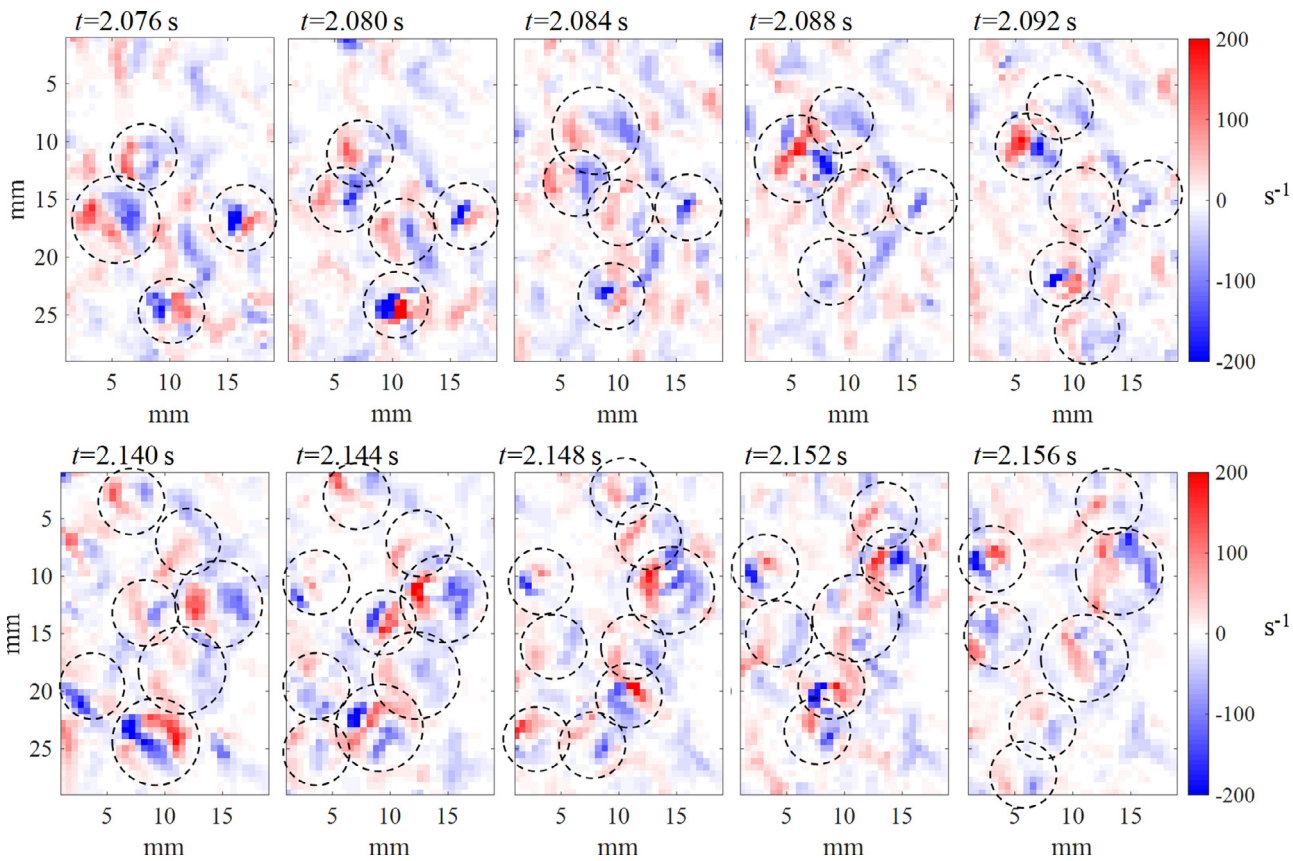

Fig. 10. Sequential distributions of instantaneous liquid vorticity from t = 2.076 s to 2.092 s (top), and from t = 2.136 s to 2.152 s (bottom) for I=15 A.

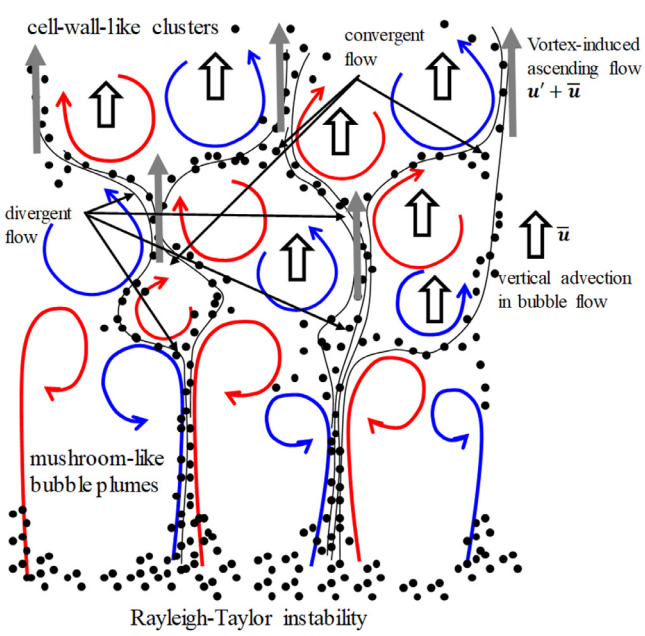

Fig. 11. Schematic illustrations of bubbles aligned on the paths in the flow induced between multiple pairs of counter-rotating vortices, forming cell-wall-like clusters; clockwise (counter-clockwise) rotations are indicated in red (blue). While the vortices are transported upward by mean bubble-induced flow with $\bar{u}$, bubbles pass around them along paths in the vortex-induced flows between the ascending vortex pairs (indicated by gray arrows). (For interpretation of the references to color in this figure legend, the reader is referred to the web version of this article.)

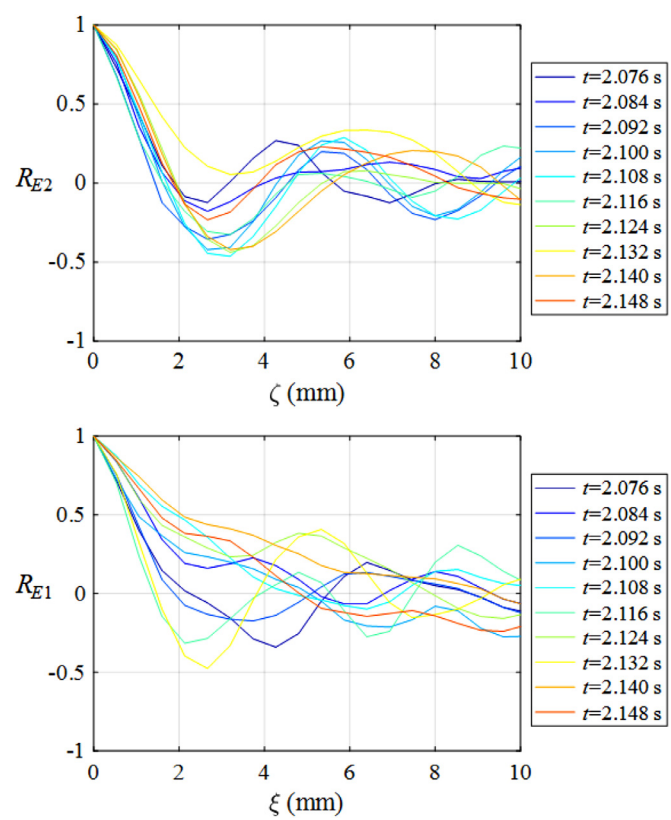

Fig. 12. Eulerian liquid velocity autocorrelations for I=15 A (see the corresponding phases in Fig. 10); R_{E2} as a function of ζ (top), and R_{E1} as a function of ξ (bottom).

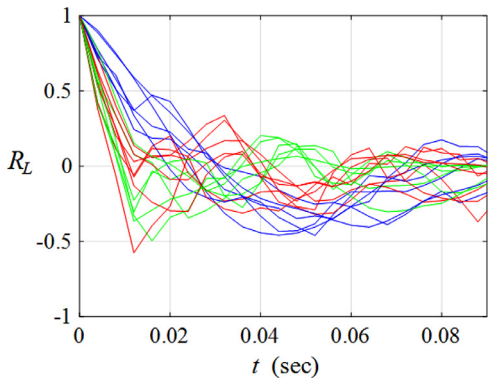

Fig. 13. Lagrangian bubble velocity autocorrelations along trajectories as a function of t for I=15 A.

tion of flows, is indicated as $\zeta = l_2^+ \sim 6$ mm where the positive correlation maxima is achieved. The ensemble averages of these two characteristic lengths are $\langle l_2^- \rangle \approx 2.96$ mm and $\langle l_2^+ \rangle \approx 5.93$ mm, respectively. R_{E1} also has similar oscillatory features characterized by time-dependent horizontal lengths (Fig. 12 bottom) having the mean values $\langle l_1^- \rangle \approx 4.26$ mm for the negative minima and $\langle l_1^+ \rangle \approx 6.16$ mm for the positive peak. Using these projected lengths, the Eulerian length scales of the organized flow structure are thus estimated as $\langle l_E^- \rangle = \sqrt{\langle l_1^- \rangle^2 + \langle l_2^- \rangle^2} \approx 5.19$ mm and $\langle l_E^+ \rangle = \sqrt{\langle l_1^+ \rangle^2 + \langle l_2^+ \rangle^2} \approx 8.55$ mm. We find the value of $\langle l_E^+ \rangle$ is consistent with the visual estimates of the separation distance of the vortex pairs (5 mm $< l_p <$10 mm, see Fig. 10) correlating with the observed unstable wavelength of the Rayleigh-Taylor instability (mean wavelength about 7 mm, see Fig. 3). The corresponding time scales of the vortex-induced flows are estimated as $T_E^- = \langle l_E^- \rangle / \overline{|\boldsymbol{u}|} \approx 0.037$ s and $T_E^+ = \langle l_E^+ \rangle / \overline{|\boldsymbol{u}|} \approx 0.061$ s, where the mean liquid velocity $\overline{|\boldsymbol{u}|} \approx 140$ mm/s.

A bubble motion relative to liquid flow is characterized by the Stokes number, $S_t = T_b/T_l$, where the bubble response time $T_b = d^2/36\nu$ and T_l is the characteristic time of the fluid motion. In the current case for I = 15 A (with the mean diameter $d = d_m$ = 0.59 mm, ν = 1.004 mm^2/s), $T_b \approx 0.010$ s. Assuming $T_l = T_E^+$ for the current vortex structure, $S_t \approx 0.157$, indicating the bubbles maintain near velocity equilibrium with the liquid flow; that is, bubbles tends to follow the vortex-induced flow and align between the vortices for forming clusters. If the bubble size is larger, for instance in case of $d = 2.0$ mm, $S_t \approx 1.815$, indicating the buoyancy-dominated bubble motion may be insensitive to the vortical liquid flows around them. Accordingly the observed distinct features of bubble flows through bubble-vortex interactions are attained only by sub-mm bubble swarms where S_t is sufficiently smaller than 1.

To detect a Lagrangian time scale along a bubble trajectory, we computed the Lagrangian velocity autocorrelation function,

$$R_L = \frac{\langle \langle v'_{bt}(t_0) v'_{bt}(t_0 + t) \rangle \rangle}{\langle \langle v'^2_{bt} \rangle \rangle} \tag{5}$$

where $v'_{bt} (= v_{bt} - \langle \langle v_{bt} \rangle \rangle)$ is the fluctuation component of tangential bubble velocity along the trajectory and $\langle \langle v_{bt} \rangle \rangle$ is the temporal mean velocity. Fig. 13 shows the Lagrangian autocorrelation for bubble velocity measured in the bubble tracking procedure. We found several similar types of oscillation behaviors with different time scales in R_L; (i) correlation maxima at $t \sim 0.03$ s and the negative minima at $t \sim 0.01$ s and 0.05 s, plotted in red lines, (ii) negative minima at $t \sim 0.01$ s and positive maxima at $t \sim$0.05 s (green lines), and (iii) longer time scale oscillation with the negative minima at $t \sim 0.05$ s (blue lines). As already discussed, in bubble flows involving multiple vortices, the bubbles locally accelerate in the vortex-induced flow between the vortex pairs and

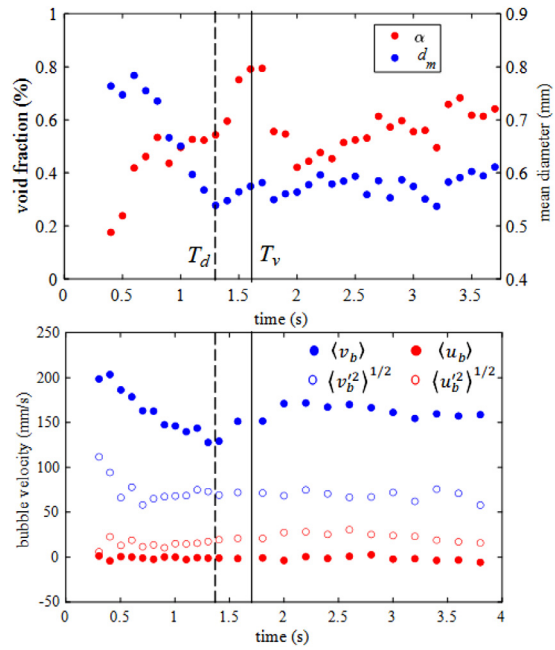

Fig. 14. Transitional void fraction α and mean diameter d_m (top), the ensemble mean horizontal and vertical bubble velocity $(\langle u_b \rangle, \langle v_b \rangle)$, and the fluctuation velocity $(\sqrt{\langle u_b'^2 \rangle}, \sqrt{\langle v_b'^2 \rangle})$ (bottom), for I = 15 A, observed in the image area of 20 mm×30 mm (see Fig. 2) at the measurement location 170 mm above the electrodes (Fig. 1).

decelerate with distance from the vortices. As the bubbles successively pass around adjacent vortex pairs during the ascending process, the possible combinations of bubble paths are constrained by relative locations with the adjacent vortices (see the bubble paths branched by divergent flows and merged by convergent ones in Fig. 11). The periodic oscillations of autocorrelation with different dominant time scales, observed in Fig. 13, indicate the different frequency of velocity variations on the different combinations of the oscillatory paths. We defined two Lagrangian time scales on the oscillatory velocity fluctuations (longer than T_b), T_L^- achieving the negative minima, and T_L^+ achieving the positive maxima, to estimate the ensemble mean time scales for each type; $\langle T_L^{(i)+} \rangle \sim$0.031s and $\langle T_L^{(i)-} \rangle \sim 0.050$ s for (i), $\langle T_L^{(ii)+} \rangle \sim 0.047$ s for (ii), and $\langle T_L^{(iii)-} \rangle \sim 0.054$ s for (iii). We find these all values are consistent with the Eulerian time scales for liquid velocity, $\langle T_E^- \rangle \sim$ 0.037 s and $\langle T_E^+ \rangle \sim 0.061$ s, which yields the evidence for bubble motion constrained by vortex-induced liquid flows through bubble-vortex interactions.

Fig. 14 presents the typical temporal variations of the void fraction α, mean diameter d_m, ensemble mean bubble velocity $\langle \boldsymbol{v}_b \rangle = (\langle u_b \rangle, \langle v_b \rangle)$, and the root-mean-square fluctuation velocity $(\sqrt{\langle u_b'^2 \rangle}, \sqrt{\langle v_b'^2 \rangle})$. In the early stage, α monotonically increases, while the bubble rise velocity $\langle v_b \rangle$ decreases with decreasing d_m. While $\langle v_b \rangle$ then change to increase after $t = T_d$ when d_m takes almost constant value, α rapidly increases to record the maximum value at $t = T_v$. This overshooting behavior of α is caused by bubble accumulation in vertical convergent flow where bubbles come up with increasing velocity from underneath after $t = T_d$. In this duration of increasing $\langle v_b \rangle$, the bubble-vortex interactions, causing local bubble acceleration, begin to intense, and the horizontal velocity fluctuation $\sqrt{\langle u_b'^2 \rangle}$ simultaneously increases. All bubble velocity components achieve statistically equilibrium state when α approaches almost constant value with fluctuations. It should be noted that increment of $\langle v_b \rangle$ from $t = T_d$ to the equilibrium state,

about 40 mm/s, has been confirmed to coincide with the value of liquid velocity fluctuation $\sqrt{\overline{\mathbf{u}'^2}}$, recorded in the same duration, indicating the direct contribution of the vortex-induced flows (with $\sqrt{\overline{\boldsymbol{u}'^2}}$) to increase the bubble velocity $\langle v_b \rangle$.

We use T_v, achieving the maximum α, as the timescale characterizing transitions of the bubble flow in the following analysis. Accordingly, introducing dimensionless time, $\tau = t/T_v$, three characteristic periods were defined as (i) the initial state in which each bubble individually rises without any bubble–bubble interaction during $0 \le \tau \le 0.5$, (ii) the transitional state in which lateral undulations of bubble motion begin to appear with varying α during $0.5 < \tau < 2$, and (iii) the statistical equilibrium state for $\tau \ge 2$.

The measured v_r, which depends on the temporal states, was compared to those from Tomiyama's drag models for a single bubble: for a pure system

$$C_{d1} = \max\left[\min\left[\frac{16}{Re}\left(1+0.15Re^{0.687}\right), \frac{48}{Re}\right], \frac{8}{3}\frac{E_o}{E_o+4}\right], \tag{6}$$

for a slightly contaminated system

$$C_{d2} = \max\left[\min\left[\frac{24}{Re}\left(1+0.15Re^{0.687}\right), \frac{72}{Re}\right], \frac{8}{3}\frac{E_o}{E_o+4}\right], \tag{7}$$

and for a fully contaminated system

$$C_{d3} = \max\left[\frac{24}{Re}\left(1+0.15Re^{0.687}\right), \frac{8}{3}\frac{E_o}{E_o+4}\right]. \tag{8}$$

It should be noted that these empirical models integrate the previous drag models and cover wide ranges of parameters, $10^{-2} < E_o < 10^3$, $10^{-14} < M < 10^7$ and $10^{-3} < Re < 10^5$.

Fig. 15 presents the transitional v_r as a function of d, together with the single bubble velocity estimated by Eqs. (6)–(8). We found that the observed velocity in the initial state ($\tau = 0.5$), indicated by blue dots, is well predicted by Eq. (7). This assures the validity of the single bubble assumption in a sodium chloride solution acting as a weak surfactant: that is, distances between adjacent bubbles are large enough in this dilute state to assume that bubble–bubble interactions are negligibly small. We also found that v_r and its variance increase (red dots at τ=1.0) until achieving the equilibrium state (black, 2.0). As discussed, counter-rotating vortices, induced by regular formations of ejections via the Rayleigh–Taylor process and transported upward by buoyancy-induced flow, contribute to locally accumulate bubbles and eject them along paths between the vortex pairs (see Fig. 11). As a consequence, our experimental results yielded greater v_r and variance compared with the models for the single bubble case, because the vortex convection locally accelerates bubble motion.

We simulated terminal v_r without bubble–vortex interaction under the current experimental conditions. For this, we used a Monte Carlo method with the drag model for a single bubble (Eq. (7)), applying it to the bubble sizes within our experiment. Fig. 16 compares the histograms of the measured v_r in the equilibrium state with the simulated ones for the lognormal random sizes following Eq. (3) (see Figs. 5 and 6). We found that the experimental v_r have symmetrical distributions, which may be approximated as Gaussian (Fig. 16 top). However, the simulated v_r without bubble–bubble interaction is characterized by an asymmetric distribution with a long tail for higher velocities (Fig. 16 bottom), clearly different in form to the experimental Gaussian distribution. According to Colombet et al. (2015), the mean v_r of swarms of needle-produced large bubbles is lower than that for single bubbles, due to the hindrance effect. We propose that the high v_r >250 mm/s in the tail of the simulated distribution for large bubbles may be retarded by this hindrance effect, reducing the tail. The observed dominant v_r, achieving the maximum frequency, is higher than the simulated one, because slower bubbles

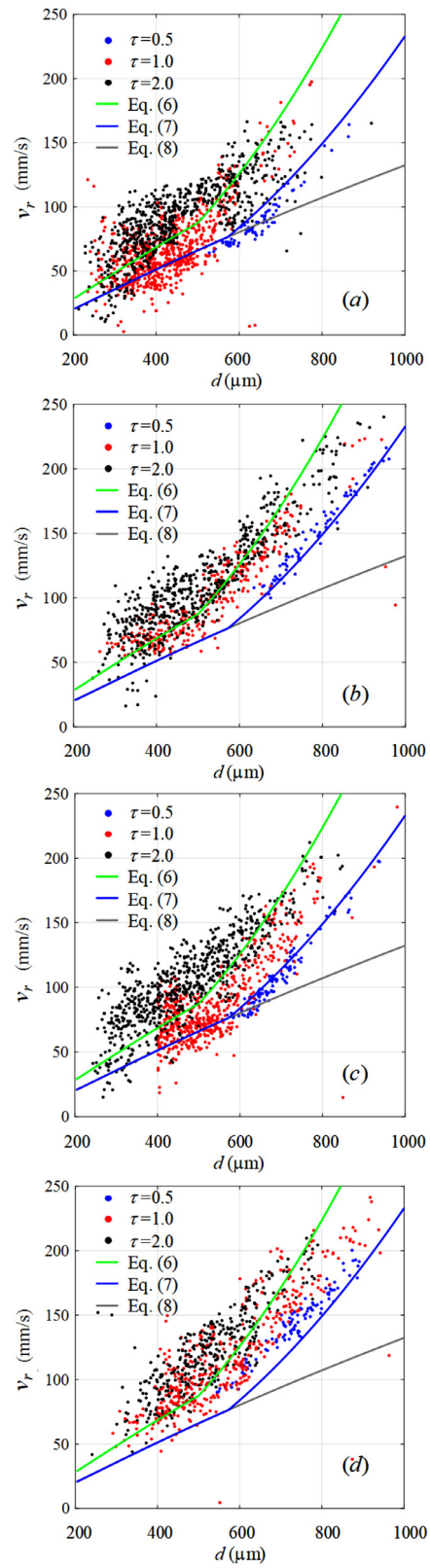

Fig. 15. Terminal bubble rise velocity in the early (τ = 0.5), transitional (1.0), and equilibrium states (2.0) as a function of bubble diameter for I = (*a*) 7.5, (*b*) 10, (*c*) 15, and (*d*) 20 A. The solid lines denote Tomiyama's model results Eqs. (6)–(8).

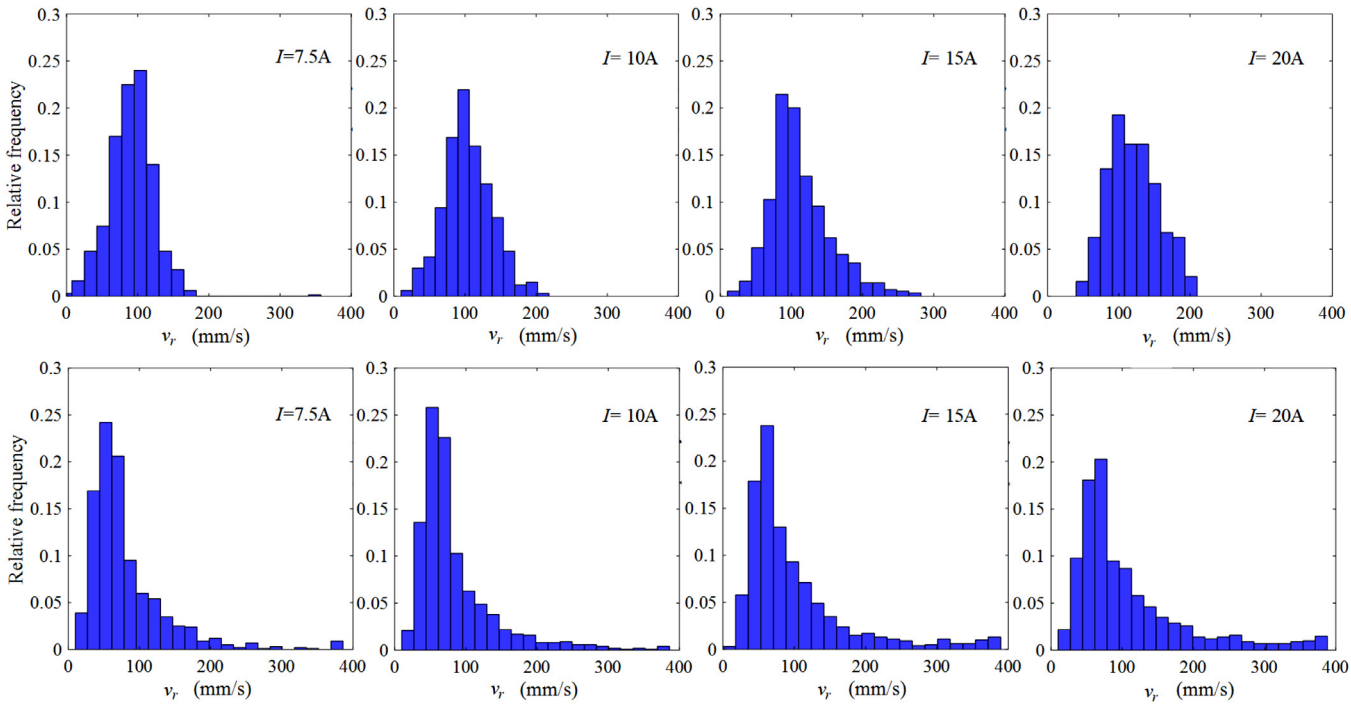

Fig. 16. Comparisons of (top) the experimental distribution of terminal velocity and (bottom) those simulated by Tomiyama model (Eq. (7)) for the optimal bubble size distribution.

are locally accelerated by upward ejections via bubble–vortex interactions (Fig. 11), as already discussed. Esmaeeli and Tryggvason (2005) computed the buoyancy-driven motion of clustered bubble swarms, characterized by a Gaussian probability density due to a diffusion process in the bubble wakes. Analogy with our measured distribution suggests that the velocity variance caused by local bubble ejections, due to vortex convection, may statistically act like macroscopic diffusion in the bubble swarm.

6. Bubble drag

In this section, we empirically determine statistical features of the experimental bubble rise to attain a drag coefficient describing the dynamics of microbubbles in swarms affected by bubble–vortex interactions.

The time-dependent $v_r(\tau)$ is assumed to take an empirical form:

$$v_r(\tau) = A(\tau)d^{n(\tau)} \tag{9}$$

where the optimal empirical variables $A(\tau)$ and $n(\tau)$ are determined by a method of least squares for all bubbles measured at a particular value of τ. If Stokes law is assumed, these empirical variables take values of $A = (\rho_l - \rho_g)g/18\mu$ and $n = 2$, where ρ_l and ρ_g are the densities of the liquid and gas, respectively. The standard deviation, σ, from the optimal v_r in Eq. (9) quantifies the variation observed in the Gaussian distributions of velocity in Fig. 16 (top).

Fig. 17 presents the temporal variations in A, n, and σ. We found that A is unstable for $\tau < 2$ until the equilibrium value, $A_e \approx 231.59$, is achieved. The exponential parameter, n, decreases from $n \approx 2$ in the initial state with low population (i.e., when the single-bubble assumption may be valid), which is identical to the value derived from Stokes drag, to the equilibrium value, $n_e \approx 1.04$, for $\tau > 2$. Accordingly, the optimal terminal v_r in the equilibrium state is given by the empirical formula:

$$v_{re} = A_e d^{n_e}. \tag{10}$$

As already discussed, the initial uniform bubble rise evolves into the complex clustered bubble behavior involved in vortex wakes, initiated by the Rayleigh–Taylor process, due to the effects of local hindrance and convective ejection, induced between vortices (Fig. 9). This rapidly increases undulations of v_r at $\tau \approx 2$, when σ achieves a statistical equilibrium at $\sigma_e \approx 20.17$ mm/s.

Fig. 18 compares v_{re} and $v_{re} \pm \sigma_e$ with the experimental data and Tomiyama's model (Eq. (7)). We found that the optimal v_{re} is an appropriate predictor of the mean measured v_r, and that the range $v_{re} \pm \sigma_e$ appropriately matches the dispersion for all cases. This leads to a probabilistic representation of v_r in terms of the equilibrium parameters, assuming a Gaussian form for the observed distribution:

$$f(v_r \mid v_{re}, \sigma_e) = \frac{1}{\sqrt{2\pi}\sigma_e} \exp\left(-\frac{(v_r - v_{re})^2}{2\sigma_e^2}\right). \tag{11}$$

The proposed probability density (Eq. (11)) may be useful for stochastically predicting bubble rise and its velocity variance in a swarm.

v_{re} (Eq. (10)) can be rewritten in terms of the bubble Reynolds number, $Re = v_{re}d/\nu$, as $v_{re} = A_e^{1/(n_e+1)}(\nu R_e)^{n_e/(n_e+1)}$, leading to an empirically determined drag coefficient, C_d, for a microbubble swarm in statistical equilibrium:

$$C_d = \frac{4}{3}\frac{\rho_l - \rho_g}{\rho_l}\frac{gd}{v_{re}^2} = \psi Re^{\phi}, \tag{12}$$

where the empirical constants $\psi = \frac{4}{3}\frac{\rho_l-\rho_g}{\rho_l} g A_e^{(\phi-1)/3}\nu^{\phi} \approx 4.35$ when $\nu = 1.004$ mm^2/s, and $\phi = \frac{1-3n_e}{n_e+1}$.

Fig. 19 presents the proposed C_d as a function of Re. C_d, which is lower than the Tomiyama model in the experimental range $20 < R_e < 200$, models a bubble-drag reduction due to bubble–vortex interactions in a microbubble swarm.

We have proposed the empirical C_d model for the electrolysis bubbles in 0.2% sodium chloride solution, categorized into a slightly contaminated system of Tomiyama model. In higher con-

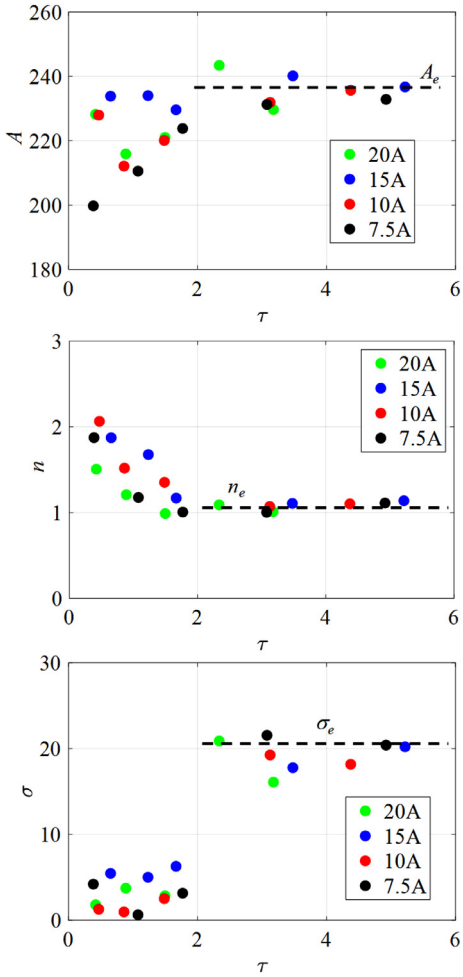

Fig. 17. Temporal variations in the optimal values of parameters (top) A, (middle) n and (bottom) σ.

centration of contamination in liquid, a well-known Marangoni effect may reduce the rise velocity of an isolated large bubble (see Fig. 15 for Tomiyama's Eq. (8), for a fully contaminated system, deviating from Eq. (7) in $d > 600$ μm). The bubble behavior and drag in swarms also depend on the surfactant species and concentration (Takagi and Matsumoto, 2011). While the model application to ocean wave filed is the final goal of this research, as stated in Section 1, a wide variety of surfactants, marine organisms, and particulates contained in seawater influence the bubble production and cause uncertainties of bubble behaviors (Slauenwhite and Johnson, 1999), which has not been considered in this study. In particular, natural occuring surfactants derived by marine planktons (Slauenwhite and Johnson, 1999) cause seasonal and regional variations of the surfactant effects through annual fluctuations of biological activities (Wurl et al., 2011), suggesting difficulties in experimentally managing surfactants in seawater. Detsch (1991) performed precise measurements of rise velocity of isolated bubbles having 20- to 1000-μm-diameter in fresh seawater, daily obtained from the St. Andrew Bay and carefully managed during the experiment. They found that all of seawater samples contained enough contamination to freeze the surface of bubbles, indicating that Eq. (8) for a fully contaminated system approximate the single bubble rise in the experimental seawater. Although seawater has not been used in the current experiments, the freezing bubble assumption followed by Eq. (8) for seawater bubbles may be acceptable to the current results for the limited tiny bubble size range $d < 600\mu$m. In addition, buoyancy-induced Rayleigh-Taylor

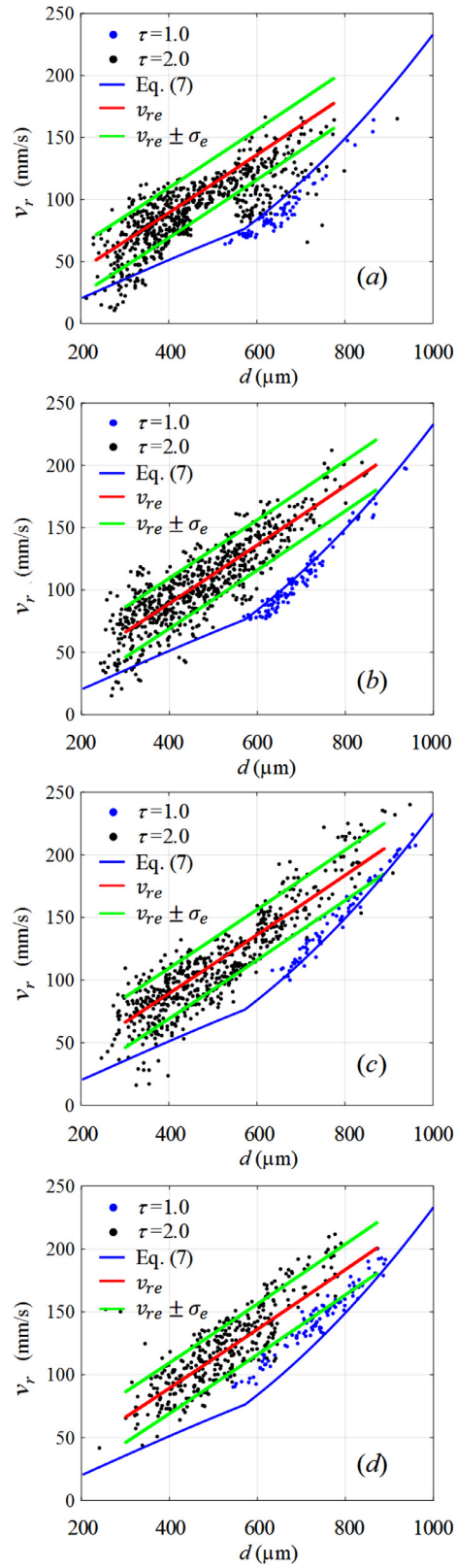

Fig. 18. Comparisons of the measured rise velocity (blue and black dots) with the proposed optimal rise velocity, v_{re} (red line), range of velocities, $v_{re} \pm \sigma_e$ (green lines), and Tomiyama's model (blue line) for currents of (*a*) 7.5, (*b*) 10, (*c*) 15, and (*d*) 20 A. (For interpretation of the references to color in this figure legend, the reader is referred to the web version of this article.)

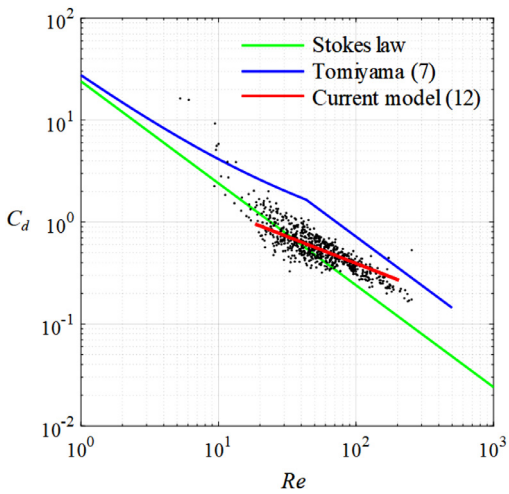

Fig. 19. The proposed drag coefficient, C_d, as a function of Reynolds number, Re with the experimental plots.

process, causing vortex formations observed in this research, likely occurs even in contaminated water where is still the difference in mean ρ between liquid and bubble layers on the electrodes. Therefore the proposed models of the rise velocity (10) and (11), and drag coefficient (12) may still be available in the limited range $d < 600\mu$m or $Re \leq 81$ for seawater. However, further research on uncertain microbubble behaviors caused by physiochemical properties of seawater is necessary for further understanding.

7. Conclusions

The transitional dynamics of electrolytically generated microbubble swarms were experimentally studied via backlit imaging and SRPIV. In the initial stage, when relative bubble population is low, uniform bubble rise along straight paths was observed in a planar bubble swarm created along the axis of the electrodes. Rayleigh–Taylor instability emerged, due to a difference in ρ, and caused buoyancy-induced vertical flows that created counter-rotating vortices, which transported ascending bubble flows. The vortex-induced flows locally accelerated bubbles and aligned them between the vortices, creating cell-wall-like bubble clusters during a transitional stage that had increasing population. Finally, the statistical features of oscillatory bubbles passing through the vortices in the convective liquid flow field attained a statistical equilibrium state. These bubble-vortex interactions in the flow involving multiple vortices, induced in the Rayleigh-Taylor process, have been supported by the Eulerian and Langangian velocity autocorrelation analyses. Accordingly the Eulerian length scales of vortex-induced flows, characterizing a separation distance between the adjacent vortex pairs, coincides with the observed unstable wavelength for the Rayleigh-Taylor instability. The Lagrangian time scales for bubble velocity correlate with the Eulerian time for liquid velocity, which supports the bubble motion synchronously varies with the vortex-induced flows.

In the statistical equilibrium state, the probability densities of microbubble sizes are well approximated by a lognormal distribution for all values of $I = 7.5$–20 A. The observed bubble size spectrum has two dominant slopes: -1.5 for a smaller than an inflection radius (300–400 µm) and -4.4 for larger a, analogous with the spectrum slopes observed in Deane and Stokes (2002). In other words, the geometrical features of the electrolytic microbubble swarm approximate well those of bubble clouds created when ocean waves break.

In the early stage of bubble generation, v_r in a swarm with a small population is described well by Tomiyama's model for an isolated bubble in quiescent, slightly contaminated water. As the population increases, mean v_r becomes larger than that estimated by Tomiyama's model and velocity variance increases, because vortex-induced liquid flows concentrate bubbles, accelerating them along paths between the vortices. A statistically steady distribution of v_r observed in the electrolytic swarm is approximated well by a Gaussian distribution, caused by the hindrance effect reducing higher v_r, while vortex convection locally accelerates lower v_r.

The optimal empirical parameters for v_r in the equilibrium state were estimated by modeling a probability density function. We also proposed a novel bubble drag coefficient for a microbubble in a swarm, in terms of these optimal empirical parameters. These models apply to the experimental range $20 < Re < 200$.

While the proposed models may help understanding mechanical contributions of microbubbles having analogous geometric features with oceanic bubbles, effects of surfactants in seawater to bubble behaviors needs to be identified for practical applications to real ocean.

Declaration of Competing Interest

The authors declare that they have no known competing financial interests or personal relationships that could have appeared to influence the work reported in this paper.

CRediT authorship contribution statement

Yasunori Watanabe: Conceptualization, Methodology, Formal analysis, Supervision, Writing - original draft, Writing - review & editing. **Haruhi Oyaizu:** Investigation, Formal analysis. **Hisashi Satoh:** Resources, Visualization. **Yasuo Niida:** Formal analysis, Validation, Visualization.

Acknowledgement

This research was supported by a JSPS Grant-in-Aid for Scientific Research (18H03791).

Supplementary material

Supplementary material associated with this article can be found, in the online version, at 10.1016/j.ijmultiphaseflow.2020.103541.

References

Callaghan, A.H., 2013. An improved whitecap timescale for sea spray aerosol production flux modeling using the discrete whitecap method. J. Geophys. Res. Atmos. 118, 9997–10010.
Callaghan, A.H., Deane, G.B., Stokes, M.D., 2012. Laboratory air-entraining breaking waves: imaging visible foam signatures to estimate energy dissipation. Geophys. Res. Lett. 43, 11,320–11,328. doi:10.1002/2016GL071226.
Callaghan, A.H., Deane, G.B., Stokes, M.D., Ward, B., 2012. Observed variation in the decay time of oceanic whitecap foam. J. Geophys. Res. 117, C09015.
Clift, R., Grace, J.R., Weber, M.E., 1978. Bubbles, Drops and Particles. Academic Press, p. 380.
Climent, E., Magnaudet, J., 1999. Large-scale simulations of bubble-induced convection in a liquid layer. Phys. Rev. Lett. 82 (24), 4827–4830.
Colombet, D., Legendre, D., Risso, F., Cockx, A., Guiraud, P., 2015. Dynamics and mass transfer of rising bubbles in a homogeneous swarm at large gas volume fraction. J. Fluid Mech. 768, 254–285.
Deane, G.B., Stokes, D.M., 2002. Scale dependence of bubble creation mechanisms in breaking waves. Nature 418, 839–844.
Detsch, R.M., 1991. Small air bubbles in reagent grade water and seawater 1. rise velocities of 20- to 1000-µm-diameter bubbles. J. Geophys. Res. 96 (C5), 8901–8906.
Esmaeeli, A., Tryggvason, G., 2005. A direct numerical simulation study of the buoyant rise of bubbles at o(100) Reynolds number. Phys. Fluids 17, 093303.
Farmer, D.M., McNeil, C.L., Johnson, B.D., 1993. Evidence for the importance of bubbles in increasing air–sea gas flux. Nature 361, 620–623.

Farmer, D.M., Vagle, S., Booth, A.D., 1998. A free-flooding acoustical resonator for measurement of bubble size distributions. J. Atmos. Oceanic Technol. 15, 1132–1146.
Jähne, B., Haußecker, H., 1998. Air-water gas exchange. Annu. Rev. Fluid Mech. 30, 443–468.
Johnson, B.D., Cooke, R.C., 1979. Bubble populations and spectra in coastal water: a photographic approach. J. Geophys. Res. 84, 3761–3766.
Keane, R.D., Adrian, R.J., Zang, Y., 1995. Super-resolution particle imaging velocimetry. Meas. Sci. Technol. 6, 754–768.
Lamarre, E., Melville, W.K., 1991. Air entrainment and dissipation in breaking waves. Nature 351, 469–472.
Melville, W.K., 1996. The role of surface-wave breaking in air–sea interaction. Annu. Rev. Fluid Mech. 28, 279–321.
Melville, W.K., Matusov, P., 2002. Distribution of breaking waves at the ocean surface. Nature 417, 58–63.
Niida, Y., Watanabe, Y., 2018. Oxygen transfer from bubble-plumes. Phys. Fluids 30, 107104.
Oguz, H.N., Prosperetti, A., 1993. Dynamics of bubble growth and detachment from a needle. J. Fluid Mech. 257, 111–145.
Otsuka, J., Saruwatari, A., Watanabe, 2017. Vortex-induced suspension of sediment in the surf zone. Adv. Water Resour. 110, 59–76.
Risso, F., 2018. Agitation, mixing, and transfers induced by bubbles. Annu. Rev. Fluid Mech. 50, 25–48.
Roghair, I., Lau, Y.M., Deen, N.G., Slagter, H.M., Baltussen, M.W., Van Sint Annaland, M., Kuipers, J.A.M., 2011. On the drag force of bubbles in bubble swarms at intermediate and high Reynolds numbers. Chem. Eng. Sci. 66, 3204–3211.
Roghair, I., Van Sint Annaland, M., Kuipers, J.A.M., 2013. Drag force and clustering in bubbles swarms. AIChE J. 59 (5), 1791–1800.
Ryu, Y., Chang, K.-A., Lim, H.J., 2005. Use of bubble image velocimetry for measurement of plunging wave impinging on structure and associated greenwater. Meas. Sci. Technol. 16, 1945–1953.
Simonnet, M., Gentric, C., Olmos, E., Midoux, N., 2007. Experimental determination of the drag coefficient in a swarm of bubbles. Chem. Eng. Sci. 62, 858–866.
Slauenwhite, D.E., Johnson, B.D., 1999. Bubble:shattering: differences in bubble formation in fresh water and seawater. J. Geophys. Res. 104 (C2), 3265–3275.
Smereka, P., 1993. On the motion of bubbles in a periodic box. J. Fluid Mech. 254, 79–112.
Squires, K.D., Eaton, J.K., 1991. Preferential concentration of particles by turbulence. Physics of Fluids A 3 (5), 1169–1178.
Takagi, S., Matsumoto, Y., 2011. Surfactant effects on bubble motion and bubbly flows. Annu. Rev. Fluid Mech. 43, 615–636.
Tomiyama, A., Celata, G.P., Hosokawa, S., Yoshida, S., 2002. Terminal velocity of single bubbles in surface tension force dominant regime. Int. J. Multiphase Flow 28, 1497–1519.
Tomiyama, A., Kataoka, I., Zun, I., Skaguchi, T., 1998. Drag coefficients of single bubbles under normal and micro gravity conditions. JSME Int. J. B 41 (2), 472–479.
Vagle, S., Farmer, D.M., 1992. The measurement of bubble-size distributions by acoustic backscatter. J. Atmos. Oceanic Technol. 9, 630–644.
Wallace, D.W.R., Wirick, C.D., 1992. Large air–sea gas fluxes associated with breaking waves. Nature 356, 694–696.
Watanabe, Y., Saeki, H., Roger, J.H., 2005. Three-dimensional vortex structures under breaking waves. J. Fluid Mech. 545, 291–328.
Wurl, O., Wurl, E., Miller, L., Johnson, K., Vagle, S., 2011. Formation and global distribution of sea-surface microlayers. Biogeoscience 8, 121–135.